Available online at www.sciencedirect.com
ScienceDirect
Earth and Planetary Science Letters 265 (2008) 287 – 301
EPSL
www.elsevier.com/locate/epsl

Anomalous cosmogenic ^{3}He production and elevation scaling in the high Himalaya

William H. Amidon [a,*], Kenneth A. Farley [a], Douglas W. Burbank [b], Beth Pratt-Sitaula [c]

[a] *California Institute of Technology, GPS Division, 1200 E. California Blvd., Pasadena, CA 91125, United States*
[b] *University of California Santa Barbara, Department of Earth Science, Webb Hall, Santa Barbara, CA 93106, United States*
[c] *Central Washington University, Department of Geological Sciences, 400 E. University Way, Ellensburg, WA 98926, United States*

Received 12 July 2007; received in revised form 10 October 2007; accepted 11 October 2007
Available online 22 October 2007
Editor: R.W. Carlson

Abstract

The production rate of cosmogenic ^{3}He in apatite, zircon, kyanite and garnet was obtained by cross-calibration against ^{10}Be in co-existing quartz in glacial moraine boulders from the Nepalese Himalaya. The boulders have ^{10}Be ages between 6 and 16 kyr and span elevations from 3200 to 4800 m. In all of these minerals ^{3}He correlates with ^{10}Be and is dominantly cosmogenic in origin. After modest correction for non-cosmogenic components, ^{3}He/^{10}Be systematics imply apparent sea-level high-latitude (SLHL) apparent production rates for ^{3}He of 226 atoms g^{-1} yr^{-1} in zircon, 254 atoms g^{-1} yr^{-1} in apatite, 177 atoms g^{-1} yr^{-1} in kyanite, and 153 atoms g^{-1} yr^{-1} in garnet. These production rates are unexpectedly high compared with rates measured elsewhere in the world, and also compared with proposed element-specific production rates. For apatite and zircon, the data are sufficient to conclude that the ^{3}He/^{10}Be ratio increases with elevation. If this reflects different altitudinal scaling between production rates for the two isotopes then the SLHL production rates estimated by our approach are overestimates. We consider several hypotheses to explain these observations, including production of ^{3}He via thermal neutron capture on ^{6}Li, altitudinal variations in the energy spectrum of cosmic-ray neutrons, and the effects of snow cover. Because all of these effects are small, we conclude that the altitudinal variations in production rates of cosmogenic ^{3}He and ^{10}Be are distinct from each other at least at this location over the last ~10 kyr. This conclusion calls into question commonly adopted geographic scaling laws for at least some cosmogenic nuclides. If confirmed, this distinction may provide a mechanism by which to obtain paleoelevation estimates.

Keywords: cosmogenic; ^{3}He; ^{6}Li; lithium; helium; apatite; zircon; kyanite; garnet; Nepal; Himalayas; paleoelevation

1. Introduction

Due to its role in determining ages and erosion rates of surfaces in the landscape, cosmogenic nuclide analysis has grown in popularity over the last several decades (Lal and Peters, 1967; Bierman, 1994; Gosse and Phillips, 2001). Although ^{3}He is not as widely applied as ^{10}Be or ^{26}Al, ^{3}He occupies a unique niche in the family of cosmogenic isotopes for several reasons. It has a higher production rate relative to its detection limit than other cosmogenic isotopes, and can thus be used to date very small samples or young surfaces. It is produced by spallation from nearly all target elements,

* Corresponding author. Tel.: +1 626 395 2190.
E-mail address: wamidon@gps.caltech.edu (W.H. Amidon).

0012-821X/$ - see front matter © 2007 Elsevier B.V. All rights reserved.
doi:10.1016/j.epsl.2007.10.022

so can potentially be applied to many different mineral phases. Because it is stable, ^{3}He is potentially useful for estimating erosion rates on extremely old surfaces, for determining exposure ages of paleo-surfaces, and for estimating catchment-scale erosion rates from ancient sediments. In addition, cosmogenic ^{3}He dating potentially provides a faster and simpler alternative to cosmogenic radionuclide dating because it does not involve intensive preparation chemistry and measurement on an accelerator mass spectrometer.

Most previous studies using ^{3}He have targeted olivine and pyroxene phenocrysts, and numerous production rate determinations for olivine have been made on basalt flows of known age, yielding sea-level high-latitude (SLHL) rates between ~100 and 150 atoms g^{-1} yr^{-1} (Kurz et al., 1990; Cerling and Craig, 1994; Licciardi et al., 1999; Dunai and Wijbrans, 2000; Ackert et al., 2003; Licciardi et al., 2006). Recent efforts have explored extending ^{3}He dating by establishing production rates and the non-cosmogenic background in additional mineral phases found in more diverse lithologies. For example, production rates of ^{3}He in apatite, zircon, titanite and Fe–Ti oxides were determined by cross-calibration against cosmogenic ^{21}Ne in Andean tuffs (Kober et al., 2005; Farley et al., 2006). Similarly, the production rate in garnet was calibrated against ^{10}Be in glacial moraine boulders from the Nepalese Himalaya (Gayer et al., 2004). In addition, Kober et al. (2005) provide estimates of element-specific ^{3}He production rates based on a combination of field calibration and neutron bombardment experiments. These estimates are useful for predicting production rates in minerals that have not been directly calibrated. However, due to complicating variables such as Li content, grain size, elevation, and lithology, further calibration studies are needed before robust and widely applicable production rates are established.

Here we calibrate the production rate of cosmogenic ^{3}He in zircon, apatite, kyanite, and garnet against ^{10}Be in quartz in a suite of glacial moraine boulders in the Nepalese Himalaya. Our approach and sampling locality are similar to the study of cosmogenic ^{3}He in garnet performed by Gayer et al. (2004). Our sample suite also allows us to assess Gayer et al.'s observations of anomalous production rates and altitude scaling of cosmogenic ^{3}He in Himalayan garnets, and a recently proposed explanation that these anomalies arise from nuclear reactions on lithium (Dunai et al., 2007).

Natural samples have multiple sources of ^{3}He in addition to the sought-after cosmogenic spallation component. With the knowledge of the Li concentration of the analyzed phases, the composition of the whole

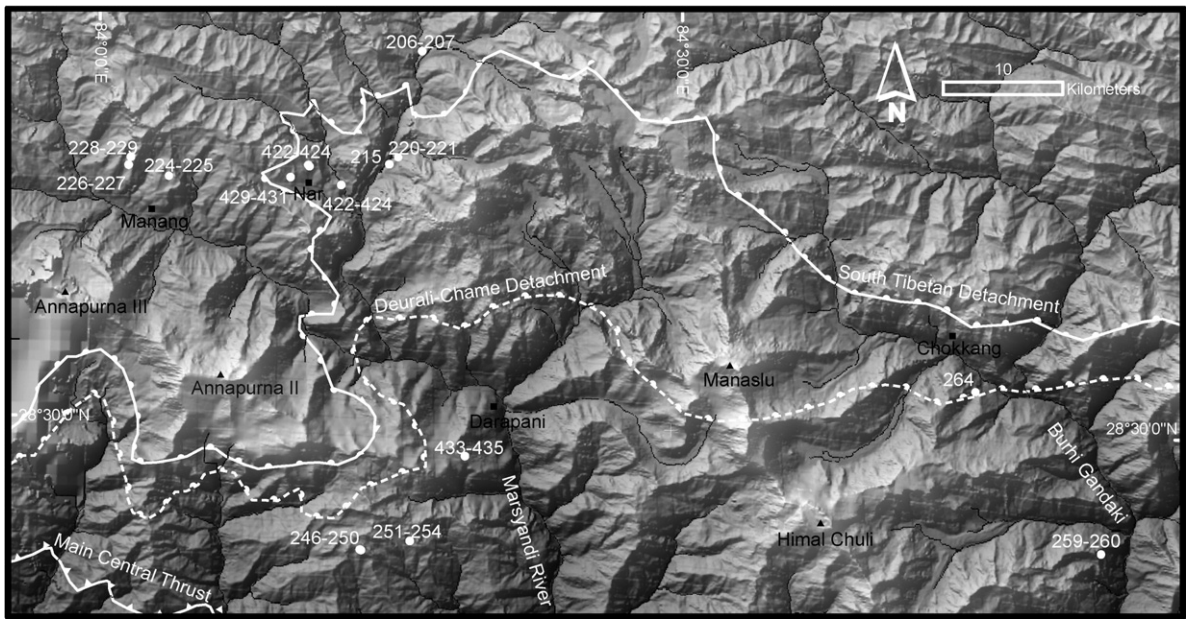

Fig. 1. Map of field area showing sample sites (white circles), towns (black squares), and major summits (black triangles). Major structural features are shown following Searle and Godin (2003), and delineate the Tethyan Sedimentary Series (north of the South Tibetan Detachment), from the Greater Himalayan Series (south of the Deurali-Chame detachment). The shaded relief map is derived from SRTM 90 m data.

rock, and appropriate models, we can isolate cosmogenic ^{3}He from these other components. SLHL production rates are then estimated by multiplying the cosmogenic ^{3}He/^{10}Be ratio by the known SLHL ^{10}Be production rate. This approach eliminates the need to assume negligible surface erosion or burial, but requires that cosmogenic isotope production rates scale identically with elevation and latitude. Unless otherwise stated, ^{3}He production in this paper refers to both direct production, and production via ^{3}H.

2. Geologic setting and samples

Field sampling and ^{10}Be analysis of glacial moraine boulders were performed by Pratt-Sitaula (2004). She sampled three types of glacial moraine boulders: quartzite, gneiss, and granite. Quartzitic moraine boulders were sampled entirely above 4000 m and contain low but variable concentrations of illite, sericite, and other clay minerals, as well as trace amounts of rutile, pyrite, and zircon. The gneissic moraine boulders were sampled between 3215 and 3960 m, and are derived from Formation I of the Greater Himalayan Series (Fig. 1). These amphibolite grade gneisses typically contain varying amounts of quartz, K-feldspar, plagioclase (albite to labradorite), muscovite and biotite. The Manaslu granite is a generally medium-grained leucocratic granite, which typically contains ~32% quartz, ~37% plagioclase (An 2-21), ~21% K-feldspar, ~7% muscovite, and ~3% biotite (Deniel et al., 1987).

Useable quantities of zircon were recovered only from the quartzitic and gneissic boulders, whereas apatites were recovered from all lithologies. Kyanites and garnet occurred only in a subset of the gneisses, and were hand-picked from the 250<500 μm size fraction (Table 3). Garnets show a narrow compositional range, averaging about 70% almandine, and 18% pyrope (Supplementary Table 2). Although the retentivity of ^{3}He in kyanite has never been demonstrated, it is a member of the nesosilicate family and is structurally similar to other retentive nesosilicates such as olivine, zircon and garnet.

Beryllium concentrations in quartz range from 0.32 to 1.3 Mat g^{-1}, interpreted as moraine ages from 5.2 to 16.3 kyr (Pratt-Sitaula, 2004). The preliminary ages listed in Tables 1–3 were calculated using the spreadsheet of Pigati and Lifton (2004), and an SLHL production rate of 5.1 atoms g^{-1} yr^{-1}. Topographic shielding was calculated following Farber et al. (2005), and snow shielding as described in Pratt-Sitaula (2004), values for both are listed in Supplementary Table 1. The wide range of ^{10}Be concentrations, moraine ages, and elevations makes this an ideal sample suite with which to assess factors controlling the cosmogenic ^{3}He production rate. Interestingly,

Table 1
Zircon data

	n	Measured ^{3}He (Mat/g)	Corrected ^{3}He (Mat/g)	^{10}Be (10^{5} at/g)	3/10 Ratio	Excess ^{3}He (Mat/g)	^{10}Be age[a] (Kyr)	Elevation (m)	U/Th–He age (Ma)	^{4}He (10^{15} at/g)	3/4 Ratio	Li (ppm)	Avg. Length (μm)	Avg. Width (μm)
Quartzite														
222	1	40.7	39.9	10.1	39.3	23.4	11.7	4614	11.5	11.5	3.1E-09	1.10	115	78
224	2	45.5	44.7	11.0	40.6	26.7	12.3	4660	13.1	11.1	3.6E-09	0.98	129	90
226	2	18.6	17.6	5.2	33.6	9.7	6.9	4500	17	3.1	5.0E-09	3.70	95	52
227	1	23.9	22.9	6.1	37.5	13.5	8	4500	16.5	14.1	1.5E-09	1.60	99	64
228	2	22.4	21.5	5.9	36.6	12.4	6.8	4744	14.9	21.1	1.1E-09	3.80	105	68
229	2	23.9	22.7	5.4	41.9	14.7	6.4	4744	20.5	10.5	1.9E-09	3.50	76	52
420	2	25.2	24.0	6.1	39.4	14.8	6.6	4821	19.6	13.6	1.9E-09	7.80	118	74
423	1	27.6	26.6	5.5	48.1	18.2	6.5	4700	14.6	10.5	2.6E-09	5.40	127	78
424	1	24.6	23.8	5.2	45.8	15.7	6.1	4700	9	14.8	1.5E-09	5.10	114	74
429	1	48.5	46.8	13.1	35.6	26.1	15.1	4600	12.7	2.4	2.0E-08	7.10	122	77
431	2	38.1	35.7	9.4	37.9	22.0	11.2	4580	41.3	17.1	2.0E-09	8.90	190	139
434	2	20.8	20.2	3.8	53.2	14.3	6.6	4057		29.1	1.6E-09	3.40	186	100
Gneiss														
246	5	22.8	22.4	6.6	34.0	11.6	11.8	3960	1.5	2.2	8.6E-09	0.20	136	86
251	2	19.7	19.0	6.0	31.4	9.4	12.8	3610	1.5	3.8	7.4E-09	0.22	168	101
259	10	10.8	10.0	3.6	27.5	4.6	11.8	3215	2	2.0	5.0E-09	0.28	133	76

[a] Approximate age. Precise ages to be published with detailed geologic context.

Table 2
Apatite data

	n	Measured ^{3}He (Mat/g)	Corrected ^{3}He (Mat/g)	^{10}Be (10^5 at/g)	3/10 Ratio	Excess ^{3}He (Mat/g)	^{10}Be age[a] (Kyr)	Elevation (m)	U/Th–He age (Ma)	^{4}He (10^{15} at/g)	3/4 Ratio	Li (ppm)	Avg. Length (μm)	Avg. Width (μm)
Granite														
206	3	49.1	43.7	9.3	47.1	28.7	13.7	4300		4.40	1.1E-08	12.5	275	207
207	2	48.1	42.7	9.1	46.9	28.1	5.2	4300		3.73	1.3E-08	13.9	282	206
215	2	26.0	22.8	6.0	37.7	12.7	12.5	3720		3.75	6.9E-09	4.3	291	212
220	3	24.3	17.9	4.7	38.4	14.1	9.1	3815	8	5.80	4.2E-09	20.3	299	225
221	3	25.2	16.7	5.0	33.5	14.3	9.7	3815	6	4.58	5.5E-09	33.4	137	90
Gneiss														
253	2	27.9	27.5	5.8	47.2	15.1	12.2	3631		0.88	3.2E-08	1.5	269	200
259	5	13.1	12.4	3.6	34.1	5.1	11.8	3215	0.8	0.33	3.9E-08	1.1	116	87
260	1	13.6	12.9	3.3	39.1	6.4	11.0	3215	1.5	0.33	4.1E-08	1.7	114	84
264	6	13.6	12.7	3.4	37.0	6.1	16.3	3450	1.5	0.21	6.5E-08	3.7	244	180
Quartzite														
433	2	17.7	17.5	3.7	46.8	9.5	6.9	4010		0.25	7.1E-08	2.0	262	200
435	2	17.4	17.2	4.0	42.9	8.6	6.9	4070		0.20	8.6E-08	1.5	263	199

[a] Approximate age. Precise ages to be published with detailed geologic context.

some moraines from similar elevations in nearly adjacent valleys yielded very different ^{10}Be ages, allowing separation of age from elevation effects. Our approach for calibration of ^{3}He production rates assumes that these ^{10}Be concentrations are accurate and purely cosmogenic in origin. We have no independent way to assess the validity of the ^{10}Be ages other than to note that they can be rationalized (Pratt-Sitaula, 2004) and other studies in central Nepal and elsewhere in the Himalaya report moraine boulders with comparable ages (Owen et al., 2005; Gayer et al., 2006).

3. Methods

Apatite and zircon were extracted from the <250 μm sieve fraction produced during original preparation for ^{10}Be analysis (Pratt-Sitaula, 2004). Standard heavy liquid and magnetic separation procedures were used,

Table 3
Kyanite and garnet data

	n	Measured ^{3}He (Mat/g)	Corrected ^{3}He (Mat/g)	^{10}Be (10^5 at/g)	3/10 Ratio	^{10}Be age[a] (Kyr)	Elevation (m)	^{4}He (10^{12} a/g)	3/4 Ratio	Li (ppm)	Width (μm)	Length (μm)
Kyanite												
246	2	22.7	NA	6.6	34.4	11.8	3960	87	2.6E-07	0.175	>500	>1000
249	2	22.3	NA	6.2	36.1	11.4	3910	79	2.8E-07	0.085	>500	>1000
251	2	20.4	NA	6.3	32.6	12.8	3610	114	1.8E-07	0.065	>500	>1000
252	1	23.6	NA	6.0	39.1	13	3625	122	1.9E-07	0.030	>500	>1000
253	2	22.6	NA	5.7	39.9	12.5	3652	166	1.4E-07	0.096	>500	>1000
254	2	19.4	NA	5.9	32.7	12.4	3640	87	2.2E-07	0.025	>500	>1000
Garnet												
247	2	25.1	19.7	6.7	29.5	12	3960	36	6.9E-07	61.6	>300[b]	>300[b]
249	2	24.4	21.6	6.2	35.0	11.4	3910	11	2.3E-06	31.3	>300[b]	>300[b]
250	2	19.6	16.2	6.3	25.6	11.7	3910	31	6.4E-07	37.9	>300[b]	>300[b]
251	4	20.5	18.3	6.0	30.3	12.8	3610	31	6.7E-07	25.2	>300[b]	>300[b]
253	2	21.7	19.5	5.8	33.4	12.5	3630	80	2.7E-07	27.6	>300[b]	>300[b]

[a] Approximate age. Precise ages to be published with detailed geologic context.
[b] Garnet samples were almost entirely composed of fragments.

followed by negative picking of contaminant mineral phases. Zircon separates were purified by dissolution of remaining phases in a room temperature solution of 2:1 HF to HNO_3. Purity of apatite was verified by recovery of the sample following helium extraction, and dissolution in 10% HNO_3. After dissolution only quartz remained, and never exceeded 1% of the analyzed mass. Typically, 3–30 mg of apatite or zircon was analyzed to generate a measurable amount of ^{3}He (usually 10^{-4} to 10^{-3} fmol), which typically corresponded to ~4 to 250 pmol of ^{4}He. Samples were degassed using either a Nd-YAG laser (House et al., 2000) or a double-walled resistance furnace, purified by diffusion through a liquid nitrogen-chilled charcoal trap and hot and cold SAES getters, then cryogenically focused and analyzed on a MAP 215-50 noble gas mass spectrometer.

The most challenging aspect of measuring cosmogenic ^{3}He in zircon and apatite is the measurement of small amounts of ^{3}He in the presence of large quantities of radiogenic ^{4}He. Issues such as variable ionization efficiency, pressure broadening of the ^{4}He and HD peaks, and scrubbing of ^{3}He off the walls of the vacuum line and mass spectrometer are all potential concerns. Although the mass spectrometer is continually calibrated using external gas standards, in-run sensitivity is determined using a "spike" of ^{3}He gas introduced midway through each sample analysis. To test for tailing and other effects of high helium pressure, we did experiments using a virtually pure ^{4}He gas derived from a sample of cosmic-ray shielded thorianite. A more detailed description of the analytical technique can be found in the online supplemental materials.

Lithium measurements were made on a Thermo-Finnegan Element 1 single-collector ICPMS, using isotope dilution with a ^{6}Li spike calibrated with a commercial Li normal solution. Measurements were made on ~1 mg of hand-picked zircon or apatite, but not the same aliquots used for ^{3}He analysis. Apatites were directly dissolved in nitric acid, whereas zircons, kyanites, and garnets were dissolved first in HF in a Parr bomb at 220 °C, then dried down and redissolved in 6N HCl at 180°, then dried down again before final dissolution in concentrated HNO_3. Reproducibility of Li measurements was established by performing at least two replicate measurements on all samples. External precision was determined by analyzing replicates of

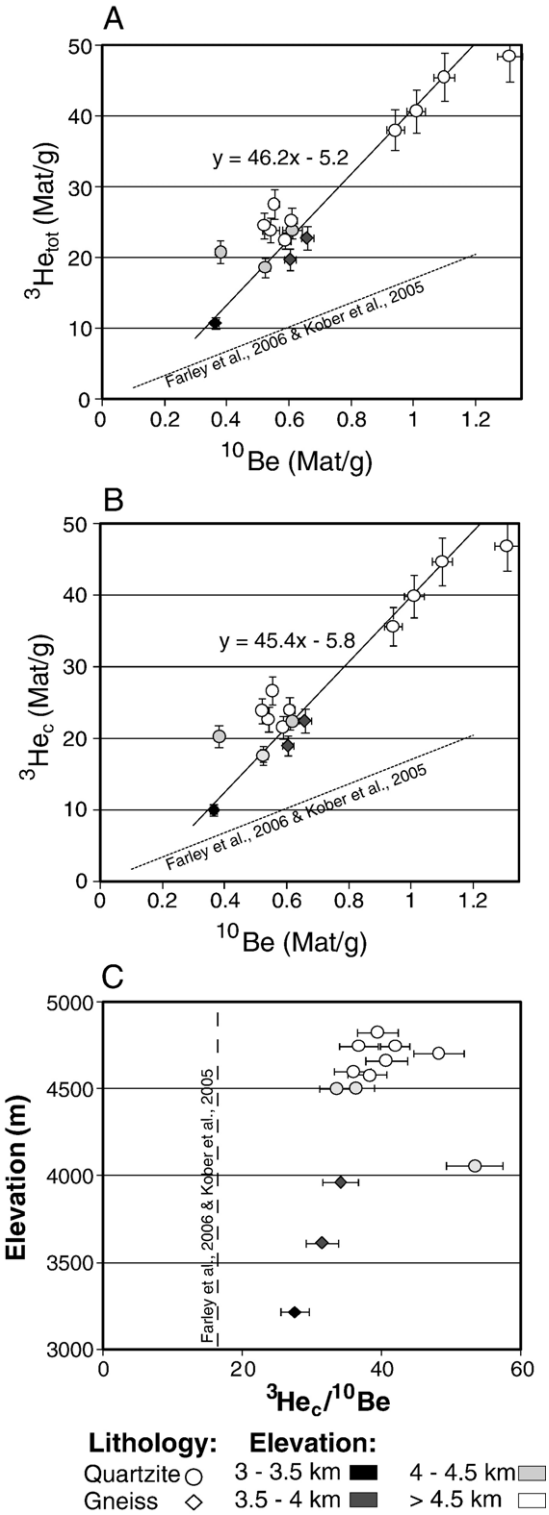

Fig. 2. A) Plot of total ^{3}He in zircon against measured ^{10}Be in quartz, with the best-fit line through the data, and the relationship predicted by Kober et al. (2005); Farley et al. (2006) (dotted line). B) Plot of spallation ^{3}He in zircon obtained by subtraction of the estimated amount of ^{3}He produced by thermal neutron capture by ^{6}Li (i.e. the $^3He_{cn}$ and $^3He_{nuc}$ components). The slope of 45.4 coupled with the known ^{10}Be production rate gives an apparent SLHL ^{3}He production rate of 226 atoms g^{-1} yr^{-1} in zircon. C) Corrected ^{3}He/^{10}Be ratios for zircon plotted against elevation, showing an increase with elevation.

~15 Durango apatite samples (Young et al., 1969), which were found to have a mean Li concentration of 1.31±0.15 ppm. Lithium blanks typically totaled less than 0.1% of measured lithium, with a maximum of ~5%.

A critical aspect of this method is ensuring that Li contamination from heavy liquids can be removed from the samples prior to analysis. This was verified by taking samples of Durango apatite which had never been exposed to heavy liquids, and immersing them for 30 min in either lithium metatungstate, methylene iodide, or acetylene tetrabromide. The samples were subsequently washed with acetone, then washed in

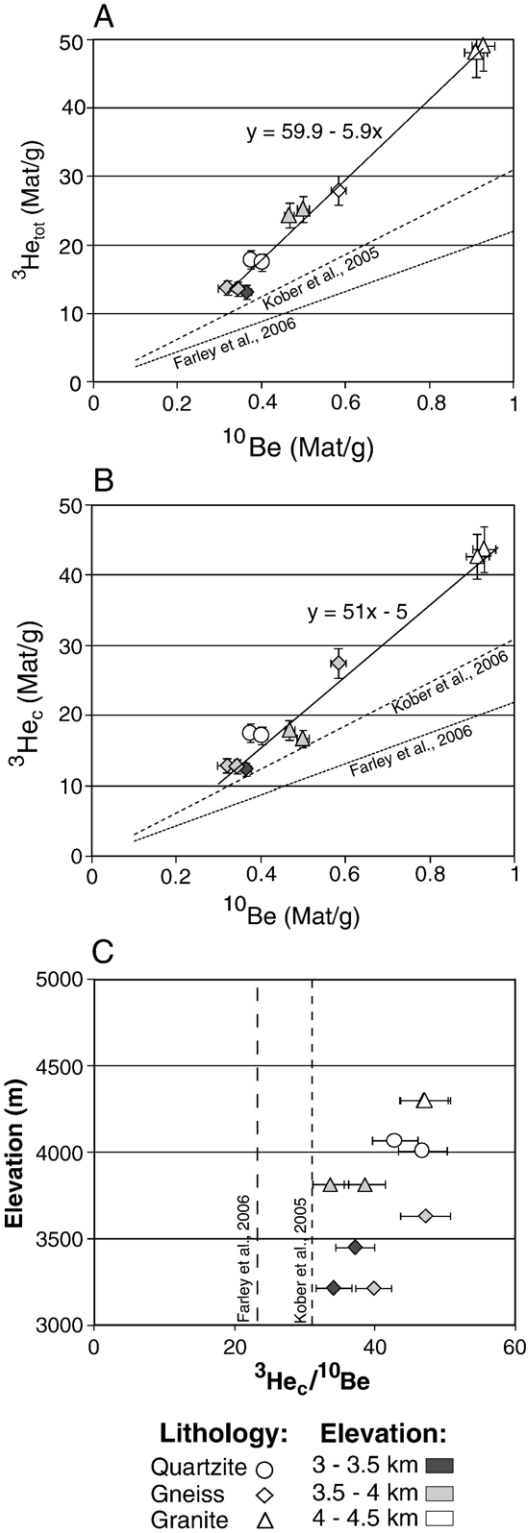

Fig. 3. A) Plot of uncorrected ^{3}He in apatite against measured ^{10}Be in quartz, with the best-fit line through the data, and the relationships predicted by Kober et al. (2005); Farley et al. (2006) (dotted lines). B) Plot of spallation ^{3}He in apatite obtained by subtraction of the estimated amount of ^{3}He produced by thermal neutron capture by ^{6}Li (i.e. the $^3He_{cn}$ and $^3He_{nuc}$ components). The slope of 51 gives an apparent SLHL production rate of 254 atoms g^{-1} yr^{-1} in apatite. C) A plot of the corrected $^3He/^{10}Be$ ratios for apatite against elevation, showing an increase with elevation.

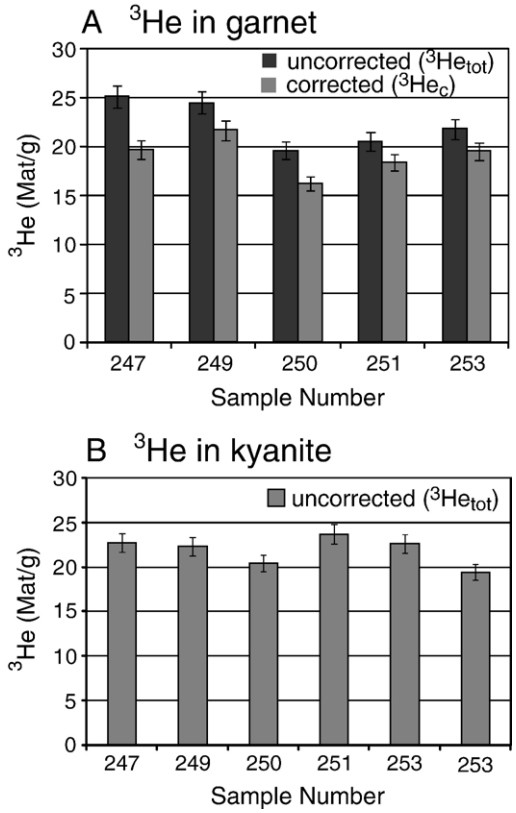

Fig. 4. A) Bar graph showing ^{3}He concentration before and after subtraction of the estimated amount of ^{6}Li produced ^{3}He in garnet with 1-sigma error bars. B) Bar graph showing measured ^{3}He concentrations in kyanite with 1-sigma error bars. No correction was made to kyanite, because of its large grain size and extremely low Li content.

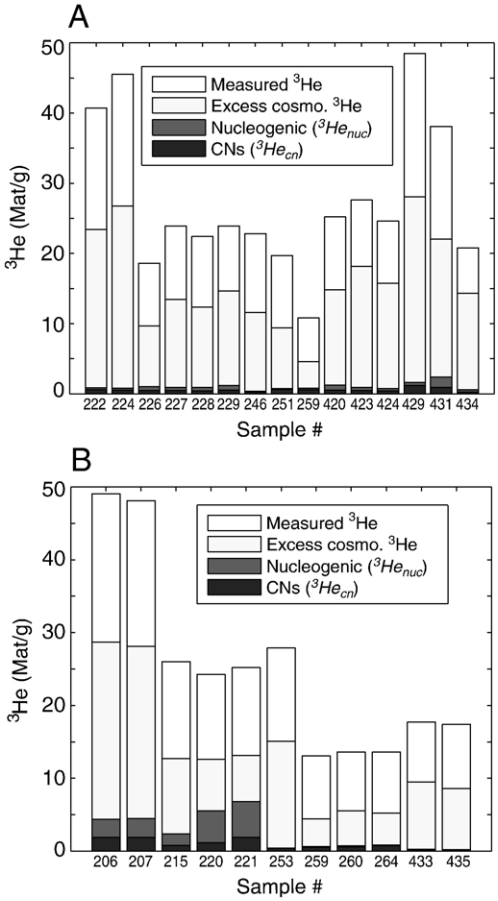

Fig. 5. Bar graph showing the estimated concentrations of ^{3}He in zircon (A) and apatite (B) from capture of low-energy cosmogenic neutrons ($^3He_{cn}$) and radiogenic neutrons ($^3He_{nuc}$) overlain on the excess cosmogenic ^{3}He (relative to Farley et al. (2006)) and the total observed ^{3}He. Note that the measured ^{3}He, excess cosmogenic ^{3}He, and $^3He_{cn}$ bars are plotted from zero, whereas the $^3He_{nuc}$ bar is stacked on top of the $^3He_{cn}$ bar because they are both produced from Li. Detailed discussion of these calculations can be found in Section 5.1.

distilled water in an ultrasonic bath for three 15 minute cycles with the water decanted and refilled between each cycle. Samples of Durango apatite exposed to heavy liquids were found to yield Li concentrations within error of the unimmersed samples. We used this cleaning procedure prior to all Li measurements.

Knowledge of the (U–Th)/He ages of the phases we are working with is useful for assessing the duration over which nucleogenic ingrowth has occurred (Farley et al., 2006). Therefore (U–Th)/He ages were measured on hand-picked, inclusion-free single apatite and zircon crystals following the method of House et al. (2000). Most of the quartzites have zircon helium ages from ~13 to 20 Ma, whereas zircons from the gneisses have ages from 1.5 to 2 Ma (Table 1). Apatite (U–Th)/He ages range from 6 to 8 Ma in the granitic samples, and from 0.8 to 1.5 Ma in the gneisses (Table 2). The correlation of age with lithology arises from the fact that lithology varies with structural position and elevation.

4. Results

4.1. ^{3}He concentrations

Helium concentrations are summarized in Tables 1–3 and Figs. 2–4. Concentrations of ^{3}He measured in apatite and zircon range from ~10 to 50 Mat g^{-1}, whereas ^{3}He concentrations in kyanite and garnet range from ~19 to 25 Mat g^{-1}. ^{4}He concentrations range from 2–40 × 10^{15} atoms g^{-1} in zircon, 0.2–6 × 10^{15} in apatite, and 11–166 × 10^{12} in kyanite and garnet. These values yield ^{3}He/^{4}He ratios ranging from 0.8–2 × 10^{-8} in zircon, 0.7–1 × 10^{-8} in apatite, and 0.69–2.5 × 10^{-6} in kyanite and garnet. The external precision of the measurements was determined by replicate analyses of 10 different aliquots of zircon from sample 259 (Table 1), as well as 10 replicate analyses of a gas standard which gave a ^{3}He signal comparable to a typical sample (2–3 cps). The standard deviation was ~8% in both cases, a value that we take as the uncertainty on a single analysis. The standard error of the sample mean for each sample is then determined by dividing this uncertainty by the square root of the number of replicate analyses for that sample. Full process blanks were measured before most analyses, resulting in blank corrections from 1 to 5%.

As shown in Figs. 2A and 3A, ^{3}He concentrations in the apatites and zircons are strongly correlated with ^{10}Be, providing unequivocal evidence that at least a large fraction of the ^{3}He in these samples is cosmogenic in origin. There is insufficient variability in the ^{10}Be measurements to make the same statement for the garnet and kyanite samples, but ^{3}He/^{4}He ratios near or in excess of the atmospheric ratio leave little doubt that cosmogenic He is present in these minerals as well.

4.2. Lithium contents

Li contents in zircon and apatite correlate strongly with host lithology. Zircons from the gneisses have Li contents of 0.17–0.30 ppm, whereas zircons from the quartzites range from ~1.6–9 ppm. The reason for this difference is unknown. Apatites from the gneisses have ~0.8–4 ppm of Li, whereas apatites from the Manaslu granite range from 4–33 ppm. In general, these are extremely high Li contents for apatite, based on analyses

of unrelated apatite samples from 8 other locations, which showed concentrations of 0.5 to 1.5 ppm (Amidon and Farley, unpublished data). In contrast, kyanites have extremely low Li concentrations, ranging from 0.03 to 0.18 ppm. Lithium concentrations in garnet range from ~25 to 62 ppm.

5. Discussion

5.1. Sources of ^{3}He in minerals

As shown in Eq. (1), the ^{3}He we measured ($^3He_{tot}$) is derived from several different sources:

$$^3He_{tot} = {}^3He_c + {}^3He_{cn} + {}^3He_{nuc} + {}^3He_{in} \quad (1)$$

We are interested in determining the production rate of cosmogenic ^{3}He (^3He_c), which includes a small component of direct muogenic production. Production can also occur via capture of cosmogenically derived low-energy neutrons ($^3He_{cn}$), which includes thermalized atmospheric neutrons, evaporation neutrons, and neutrons produced by stopping of slow and fast muons (Dunai et al., 2007). A third term is nucleogenic ($^3He_{nuc}$) production, which refers to ^{3}He produced by capture of radiogenic neutrons and by ^{238}U fission. Finally, some minerals may contain inherited ^{3}He ($^3He_{in}$) in inclusions or from prior exposure. In this section, we will estimate $^3He_{cn}$, $^3He_{nuc}$, and $^3He_{in}$ and subtract them from the measured $^3He_{tot}$ to determine ^3He_c in our samples.

The $^3He_{cn}$ component is derived from capture of cosmogenically derived low-energy (<1 KeV) neutrons (CNs): $^6Li(n,\alpha)^3H \rightarrow {}^3He$ (Mamyrin and Tolstikhin, 1984; Lal, 1987). Estimating the $^3He_{cn}$ component requires the Li content in the mineral, and the CN stopping rate in the rock. To calculate the CN stopping rate, we used the equations of Phillips et al. (2001). Both the absolute CN stopping rate and its profile with depth in rock depend heavily on concentration of neutron-absorbing and moderating elements such as H, B, Li, Cl, Mn, Sr, Cd, and REEs (Friedlander et al., 1981; Phillips et al., 2001). Typical neutron fluxes and other calculated parameters for rocks in this study are included in Supplementary Table 3.

Because we only obtained the <250 μm size fraction of the samples, and no hand samples were preserved, we were unable to measure bulk rock elemental compositions. Instead, we used the composition of the IGGE sandstone GSR-4 (Potts et al., 1992) as the bulk rock composition of quartzite, and used published compositions measured from nearby locations in the Himalaya for granite and gneiss (Le Fort, 1981; Colchen et al., 1986; Brouand et al., 1990; Guillot and Le Fort, 1995; Barbey et al., 1996). Bulk compositions used in our calculations are given in Supplementary Table 4. Li contents of 11 ppm for quartzite (measured in quartz), 20 ppm for gneiss (Brouand et al., 1990), and 60 ppm for granite (Barbey et al., 1996) were adopted. The concentration of Li in the mineral of interest was measured (Tables 1–3). To calculate $^3He_{cn}$ we convert the total neutron stopping rate (R_{cn}) into a neutron stopping rate on Li (Andrews and Kay, 1982) by multiplying by the fractional absorption cross section of Li in the rock (F_σ). This quantity is then multiplied by the ratio of the Li concentration in the mineral to that in the bulk rock to yield the production rate from Li in the mineral (P_{cn}).

$$P_{cn} = R_{cn} * F_\sigma * \left(\frac{C_{min}}{C_{rock}}\right) \quad (2)$$

After an identical calculation is made to determine the production rate in the whole rock, the effect of implantation and export of ^{3}He produced in-situ and in the neighboring minerals is considered. This is done by calculating the apparent production rate in the mineral, following Farley et al. (2006):

$$P_a = P_i\left[1 - 0.75\left(\frac{S}{R}\right) + 0.625\left(\frac{S}{R}\right)^3\right] + P_h\left[0.75\left(\frac{S}{R}\right) - 0.625\left(\frac{S}{R}\right)^3\right] \quad (3)$$

This equation assumes a spherical geometry to calculate the apparent production rate of nucleogenic ^{3}He in the crystal (P_a), by considering the in-situ production rate in the crystal of interest (P_i), the in-situ production rate in the adjacent neighbors (P_h), the stopping distance of the particle (S), and the radius of the crystal (R) (Dunai and Wijbrans, 2000; Farley et al., 2006). We assume that the neighbors have, on average, the Li concentration of the whole rock. The apparent ^{3}He production rate (P_a) is then multiplied by the exposure age of the surface (from ^{10}Be) to determine $^3He_{cn}$.

Calculating the nucleogenic ^{3}He production ($^3He_{nuc}$) follows an identical process, except that estimates of the radiogenic neutron (RN) flux and the (U–Th)/He closure age are used (Farley et al., 2006). Radiogenic neutrons come primarily from (α,n) reactions on light elements such as Al and Mg. The RN flux was calculated following Andrews and Kay (1982) and

Chmiel et al. (2003) and is likely an overestimate due to the assumption of compositional homogeneity, when in reality, much of the α flux from U and Th rich minerals is stopped before it enters minerals rich in light elements (Farley et al., 2006). Based on published values (Brouand et al., 1990; Potts et al., 1992; Barbey et al., 1996), U contents of 2.1, 2.5, and 10 ppm were used for the quartzites, gneisses and granites respectively, and Th contents of 7, 10, and 5 ppm respectively. Nucleogenic ^{3}He can also be produced by ternary fission of ^{238}U, but this is negligible (Farley et al., 2006).

Our model calculations appear to be relatively insensitive to most of our assumptions regarding bulk rock composition. For example, doubling the U and Th contents of the host rock has a negligible effect on ^{3}He production from RNs. Likewise, doubling the Li content of the whole rock has a small affect on production of ^{3}He from CNs. This is due in large part to the assumption that the host mineral has the same Li content as the host rock, creating a tradeoff between a reduction in the total neutron flux in the rock with an increase in the stopping rate on Li in the host mineral. If this assumption is violated, it could have a strong effect on CN produced ^{3}He. However, as discussed in Section 5.3, the robust relationships and relatively few outliers observed in the data suggest this is unlikely.

We assume that the inherited ^{3}He component ($^3He_{in}$) is negligible for several reasons. First, inheritance from "recent" prior exposure (e.g. reworked moraine material) should be irrelevant due to the long half life of ^{10}Be. Inheritance from "ancient" prior exposure (e.g. prior to deposition of the meta-sedimentary rock) is unlikely because apatite, kyanite and garnet are not detrital in origin, and the quartzites have been heated to peak metamorphic temperatures of 340–400 °C (Schneider and Masch, 1993; Garzanti et al., 1994). Complete diffusive helium loss is also confirmed by the young (U–Th)/He ages of zircons in this study, relative to their Paleozoic and Proterozoic U–Pb ages (Gehrels et al., 2003). Excess ^{3}He in fluid inclusions is unlikely because the minerals used in this study are not rich in fluid inclusions and are not derived from a mantle source rich in ^{3}He.

5.2. Calculating cosmogenic ^{3}He production rates

Results of the above calculations are summarized in Fig. 5. We estimate that CN production from ^{6}Li ranges from 0.15 to 2.4 Mat g^{-1} of ^{3}He in apatite, 0.23 to 1.2 Mat g^{-1} in zircon, 0.75 to 4.6 Mat g^{-1} in garnet, and 0.13 to 0.16 Mat g^{-1} in kyanite. Likewise, we estimate that ^{3}He production from RNs ranges between 0.03 and 6.1 Mat g^{-1} in apatite, 0.12 to 1.5 Mat g^{-1} in zircon, 0.35 to 0.80 Mat g^{-1} in garnet, and ~0.026 Mat g^{-1} in kyanite. $^3He_{cn}$ and $^3He_{nuc}$ combined typically represent only about 2 to 7% of total ^{3}He in zircon, 1 to 25% in apatite, 10 to 21% in garnet, and ~0.6% in kyanite (Fig. 5). Production of ^{3}He from muon derived neutrons was calculated following Lal (1987); Heisinger et al. (2002) and found to be negligible.

As an initial attempt to calculate the production rate of cosmogenic ^{3}He, we subtracted the $^3He_{cn}$ and $^3He_{nuc}$ components from the measured $^3He_{tot}$, and then performed an error-weighted total least-squares regression of ^{10}Be vs. ^3He_c, taking the slope of the resulting line as the average $^3He_c/^{10}$Be ratio for all samples (Figs. 2 and 3). This ratio is then multiplied by a time-averaged ^{10}Be SLHL production rate of 4.98±0.34 atoms g^{-1} yr^{-1} (Balco and Stone, in review) to get the SLHL ^3He_c production rate. Importantly, this implicitly assumes that ^3He_c and ^{10}Be are produced in a constant ratio through time and over a range of elevations, as in most scaling models (Lal, 1991; Pigati and Lifton, 2004). As we discuss below, this assumption is not met, so these initial production rate estimates must be treated with skepticism. The 2-sigma errors on the ^3He_c production rates are from the error on the slope of the linear fit propagated in quadrature with the uncertainty on the SLHL ^{10}Be production rate. As discussed by Farley et al. (2006), long stopping distances can lead to net import of spallation ^{3}He into phases with small grain sizes. Following that work, the approach used here leads to "apparent" production rates (i.e., including both in-situ produced and net injected ^{3}He).

A linear fit to the zircon data (Fig. 2B) yields a slope of ~45.4±7.8 with an intercept of −5.8±4.1 corresponding to a SLHL ^{3}He production rate of ~226±39 atoms g^{-1} yr^{-1}. For apatite (Fig. 3B), the corrected data give a slope of ~51.0 and an intercept of −5.0±5.2, which corresponds to a SLHL ^3He_c production rate of ~254±60 atoms g^{-1} yr^{-1} (Fig. 3C). The production rates estimated here are ~3 times higher than observed by Farley et al. (2006) for zircon, and ~2.3 times higher for apatite.

Because the range of ^{10}Be concentrations for garnet and kyanite is limited, we use the error-weighted mean $^3He_c/^{10}$Be ratios rather than fitting a line to the points. Due to the large grain size and low Li content in kyanite, no correction for non-cosmogenic ^{3}He is made, giving a SLHL production rate of 177±24 atoms g^{-1} yr^{-1}. Correction for the non-cosmogenic ^{3}He component in garnet gives a $^3He_c/^{10}$Be ratio of ~30.8±7.2, corresponding to a production rate of 153±35 atoms g^{-1} yr^{-1}. This number is within error of the 154 atoms

g^{-1} yr^{-1} that we recalculate from the data of Gayer et al. (2004) in Section 6.2.

5.3. Limited importance of non-cosmogenic ^3He

Because production rates in this study are higher than previously observed (Farley et al., 2006), we must consider whether we have somehow underestimated non-cosmogenic sources of ^3He. The strong linear relationship between uncorrected $^3He_{tot}$ in zircon and apatite and ^{10}Be in quartz, and the near-zero intercepts of the fitted lines demonstrates that ^3He in these samples is primarily produced by spallation (Figs. 2A and 3A). This conclusion is supported by the absence of a correlation between Li content and uncorrected $^3He_{tot}/^{10}Be$ ratio, either within mineral groups or between them. Likewise, no correlation was discovered when a step-wise multiple linear regression model was constructed in which Li content, exposure age, (U–Th)/He closure age, lithology, and grain size were sequentially added as predictor variables and regressed against $^3He_{tot}/^{10}Be$ ratio. The lack of correlation between Li content and uncorrected $^3He_{tot}/^{10}Be$ ratio is particularly important for garnet, because its large grain size and high Li content make its corrected ^3He concentration insensitive to the assumed Li concentration of the host mineral. Further evidence for a small contribution of Li-produced ^3He comes from the fact that kyanite and garnet have similar $^3He_{tot}/^{10}Be$ ratios, despite three orders of magnitude higher Li contents in garnet, and otherwise similar compositions, grain sizes and host rocks.

A puzzling observation of our study is that production rates in kyanite and garnet are significantly lower than in apatite and zircon, despite predictions based on element-specific production rates that suggest they should be higher. We can use our observed production rate in kyanite to calculate element-specific production rates for Al, Si, and O if it is assumed that the ratio of production rates between these elements matches those predicted by Kober et al. (2005) and Masarik (2002). This is an appropriate assumption because the two models agree well, predicting that 14–16% of production derives from Si, 29–31% from Al, and 55% from O. Using these values, we predict 153, 159, and 197 atoms g^{-1} yr^{-1} for Si, Al, and O.

If estimates for Si and O are combined with the observed production rate in zircon, an element-specific production rate of ~270 atoms g^{-1} yr^{-1} is calculated for Zr. The production rate from this element has not been established, but our value is far higher than other elements which have been tabulated (Masarik, 2002; Kober et al., 2005) and seems implausible. One possible explanation is implantation of spallation produced ^3He from adjacent minerals, which would affect smaller grain sizes (e.g. apatite and zircon) more severely. However, this explanation is unlikely for three reasons. First, grain-size experiments run on samples 259 and 431 show no significant difference in $^3He_{tot}$ concentration between samples with average grain sizes of ~65 and 168 μm for sample 431, and only a ~15% difference was observed between average grain sizes of ~36 and 98 μm for sample 259 (Fig. 6). Second, Farley et al. (2006) did not see elevated ^3He production in apatite or zircon of only slightly larger size than used in this experiment, and observed only ~10% increase in ^3He concentration over a two-fold range in grain size. Most importantly, even if *all* of the ^3He in our zircon and apatite samples were implanted by spallation in adjacent crystals, the observed production rate is still much higher than the ~177 atoms g^{-1} yr^{-1} we would expect for quartz using our estimates for Si and O given above. Production rates in other rock-forming minerals would not be expected to differ from quartz by more than ~5% (Farley et al., 2006). As discussed below, the higher production rates in zircon and apatite than in garnet and kyanite is most likely a result of an unexpected correlation of $^3He_c/^{10}Be$ ratio with elevation coupled with the fact that on average the garnets were sampled at a lower elevation than the zircons.

5.4. Increasing ^3He production rate with elevation

Because both ^3He and ^{10}Be are produced primarily by neutron-induced spallation, both production rates are

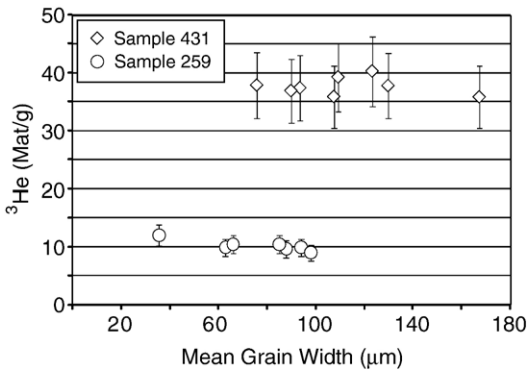

Fig. 6. Results of ^3He measurements made on different grain-size aliquots of zircon from sample numbers 259 and 431. Error bars show the 2-sigma external error discussed in the text. No relationship is observed between ^3He concentration and grain size for sample 431, and only the smallest grain-size aliquot for sample 259 (~36 μm width) shows a moderately higher concentration.

commonly assumed to scale with the atmospheric neutron flux, and the $^3He_c/^{10}Be$ should be invariant with elevation (Gayer et al., 2004). However, our results show that $^3He_c/^{10}Be$ increases with elevation in both zircon and apatite (Figs. 2C and 3C). This trend is particularly striking because it agrees very well with similar observations by Gayer et al. (2004) on Himalayan garnets. For example, although our garnet samples span a limited elevation, their $^3He_{tot}/^{10}Be$ ratios plot exactly on the predicted relationship between $^3He/^{10}Be$ and elevation shown in Figure 8 of Gayer et al. (2004). If this elevation trend reflects variations in cosmogenic production, it would require that ^3He production rate scales differently with elevation than ^{10}Be, a hypothesis discussed in Section 6.

Regardless of the origin of the elevation correlation, its existence has implications for estimation of SLHL production rates. Because samples from higher elevations often have higher ^{10}Be concentrations, the correlation tends to rotate the ^3He_c vs. ^{10}Be correlation line counterclockwise. This may account for the negative y-intercepts in Figs. 2B and 3B. More importantly it calls into question our approach to estimating ^3He production rates, and may account at least partially for the anomalously high SLHL ^3He production rates.

We can accommodate this effect in determining SLHL production rates by performing a least-squares regression that allows the $^3He_c/^{10}Be$ ratio to vary with elevation:

$$^3He_c/^{10}Be = R_o * \exp\left(\frac{Z}{Z^*}\right) \quad (4)$$

where Z is sample elevation (km), Z^* is the characteristic length scale (km) of the difference in production rate of the two nuclides, and R_o is the $^3He_c/^{10}Be$ production ratio at sea level. The justification for this formulation is that cosmogenic production rates scale exponentially with elevation (Lal and Peters, 1967); if two isotopes scale differently with elevation, then their ratio is also likely to scale exponentially. Note that if Z^* is infinite, the two isotopes scale identically with elevation and Eq. (4) reduces to the simple approach for determining production rates described in Section 5.2.

In the case of zircon, $R_o = 13.0$ at ^3He/at ^{10}Be at sea level, and $Z^* = 4.2$ km. For apatite, $R_o = 16.6$ at ^3He/at ^{10}Be and $Z^* = 4.2$ km. As shown in Supplementary Fig. 1, the resulting correlations between ^3He_c measured and modeled are excellent for both phases, providing further justification for the form of Eq. (4). The fact that two mineral phases yield almost identical values for Z^* suggests that the elevation correlation is not an artifact of inadequate correction for non-cosmogenic ^3He. Using these values for R_o, we obtain SLHL production rates of 65 atoms g^{-1} yr^{-1} for zircon and 83 atoms g^{-1} $yr^{-1}$for apatite. If kyanite and garnet follow the same elevation dependence, then their SLHL production rates are 73 and 72 atoms g^{-1} yr^{-1}respectively. These SLHL production rates are far lower than obtained without attempting to accommodate the elevation correlation. In addition, this approach at least partially explains the observation that the production rate in zircon exceeded that in garnet when ignoring the elevation correlation: because on average the zircons come from higher elevations than the garnets, the elevation effect was greater on the zircons than on the garnets. These SLHL production rates and $Z^* = 4.2$ km provide an approach for estimating ^3He production rates at any elevation. Gayer et al. (2006) provided a similar approach based on their more limited garnet data.

Eq. (4) can be rearranged to estimate elevations based solely on measured $^3He_c/^{10}Be$ ratios. Supplementary Fig. 2 shows a strong linear correlation ($R^2 = 0.68$) between the elevation implied by the $^3He_c/^{10}Be$ ratio and the known elevation of each sample in the combined apatite and zircon data set. The standard error of the elevation estimate is ~0.4 km. If the robustness of this relationship, especially its validity through time and space, can be established, it may provide a new method for reasonably precise paleoelevation estimates.

6. Possible causes of anomalous production rates

6.1. Altitudinal variations in the neutron energy spectrum

One hypothesis to explain elevated ^3He production at high elevations is that the neutron energy spectrum becomes increasingly energetic with altitude, somehow favoring increased production of ^3He over ^{10}Be (Gayer et al., 2004). This could happen because ^{10}Be and ^3He have different excitation functions, causing their production rates to respond differently to changes in the neutron energy spectrum. It is important to note that this hypothesis does not require changes in scaling of the overall neutron flux, only that the flux of high-energy neutrons increases with elevation relative to flux in other parts of the energy spectrum. Although atmospheric energy spectra do show an increasing high-energy "tail" between 100 and 10^4 MeV, where flux increases 2–3 times more rapidly with elevation than other parts of the spectrum (Goldhagen et al., 2002), previous studies do not report greatly increased

^{3}He production at high elevation (Blard et al., 2006; Farley et al., 2006). However the study of Kober et al. (2005) observes production rates in Fe–Ti oxides at >4000 m that are higher than expected relative to the accepted values for olivine and pyroxene.

Another way to test this hypothesis is to estimate ^{3}He and ^{10}Be production rates at different elevations using the neutron energy spectrum and excitation functions for production of ^{3}He and ^{10}Be. In general, excitation functions for neutron-induced reactions are poorly known for ^{3}He, necessitating the use of excitation functions for proton interactions. However, the lack of cross section data for proton-induced ^{3}He production from oxygen is a critical limitation in making mineral-specific calculations (Leya et al., 2000b). Additionally, although it is often assumed that neutron and proton excitation functions are similar for a given reaction, this is not necessarily the case (Leya et al., 2000a).

As an alternative to mineral-specific calculations, we estimate ^{3}He and ^{10}Be production rates for pure magnesium, aluminum, and silicon as a function of elevation to see if the ^{3}He/^{10}Be production ratio in these common rock-forming elements increases with elevation. The proton excitation functions for these reactions are compiled from Bodemann et al. (1993); Michel et al. (1995); Schiekel et al. (1996); Leya et al. (1998, 2000a, b), and are shown in Fig. 7B. To predict the neutron flux and energy spectrum at each elevation, we use the analytical equations of Sato and Niita (2006), calculated with a rigidity cutoff of 14 GeV, zero water content, and a moderate solar modulation of 1000 MV (Fig. 7A). We use linear interpolation of the experimentally observed cross sections to create a discretized excitation function between 10 and 2600 MeV. Next, the discretized excitation function is multiplied by the discretized energy spectrum for each elevation, and the resulting functions are numerically integrated to obtain elemental production rates at various elevations. We did not include the portion of the neutron flux above 2600 MeV in our calculation due to unknown cross sections in this region. However, because such a small portion of the total neutron flux occurs above 2600 MeV, calculations using a linear extrapolation to approximate the excitation function between 2600 and 10^4 MeV do not yield significantly different results. Our calculations show that the ^{3}He/^{10}Be production ratio actually decreases with elevation in all three elements because the shape of the ^{10}Be excitation function dictates that relatively more of the ^{10}Be production occurs in the high-energy part of the spectrum than for ^{3}He (Fig. 7C). If this relationship holds true for other elements, most importantly for oxygen, it would suggest that an increase in the high-energy neutron component with elevation would actually lead to lower ^{3}He/^{10}Be ratios. Indeed if the energy spectrum varies in time or space, it is hard to imagine that the ^{3}He/^{10}Be ratio will remain constant.

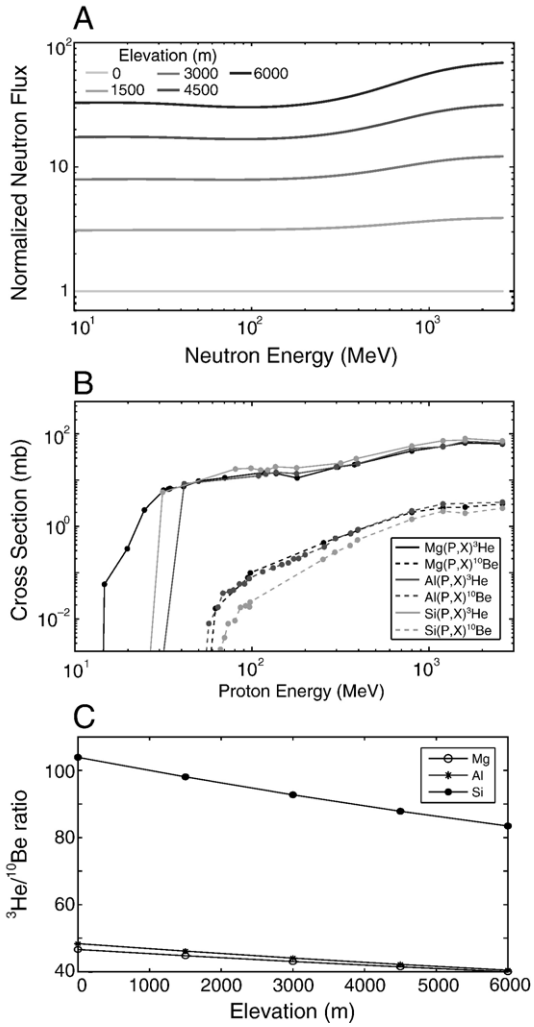

Fig. 7. Results of calculations performed to test the hypothesis that an increase in the high-energy neutron flux relative to other parts of the energy spectrum could cause the cosmogenic ^{3}He/^{10}Be ratio to vary with elevation. A) Neutron energy spectra at different elevations (see Section 6.1) normalized to the sea-level spectrum, as predicted by the equations of Sato and Niita (2006). B) Excitation functions for production of ^{3}He by proton interactions with Mg, Al and Si (Bodemann et al., 1993; Schiekel et al., 1996; Michel et al., 1997; Leya et al., 1998; Leya et al., 2000b). Dots represent actual measurements taken from the literature, lines are the interpolations used in our calculations. C) Estimated ^{3}He/^{10}Be production ratios from pure Mg, Al and Si at a range of elevations.

An alternative hypothesis presented by Gayer et al. (2004) suggests that increased ^{3}He production with

elevation could occur if high-energy neutrons induce an initial spallation event in the rock, from which the resultant tertiary neutrons retain enough energy to induce additional spallation of ^{3}He, but not of ^{10}Be (Gayer et al., 2004). Because the experimental cross sections used in this calculation are measured in foils, and not in real rock, our calculation does not explicitly test this hypothesis, although it seems reasonable given that ^{3}He production cross sections in the 10–100 MeV range are significantly larger than for ^{10}Be (Fig. 7B).

6.2. The effect of snow cover

An alternate hypothesis for elevated ^{3}He production rates is an elevated low-energy neutron flux at the rock surface due to snow cover. This occurs because covering the surface reduces the diffusive loss of thermal neutrons from the rock into the air, a process that normally reduces the low-energy neutron flux in the upper ~20 cm of unshielded rock. However, because increased low-energy neutron flux can only drive ^{3}He production by thermal neutron capture on ^{6}Li, this hypothesis would also predict that ^{3}He production in rocks with similar exposure histories should correlate with Li content in the minerals, which it does not. Similarly, in most of our kyanite and zircon samples, the concentration of Li is too low for an increased thermal neutron flux to be important.

However, snow cover is part of the reasoning used by Dunai et al. (2007) to recalculate the ^{3}He production rate observed in Himalayan garnet by Gayer et al. (2004): they attribute a substantial amount of ^{3}He production to neutron capture on ^{6}Li and thereby reduce the high cosmogenic production rate. We suspect the calculations of Dunai et al. overestimate the magnitude of the effect, and for this reason, along with the absence of a correlation between ^{3}He/^{10}Be and Li in our samples, we suggest it does not account for our high production rates and lower atmospheric attenuation length.

Neither the commonly used CHLOE model (Phillips and Plummer, 1996), nor the model of Phillips et al. (2001) can accurately predict the effect of overlying snow or ice on the low-energy neutron flux, so Dunai et al. (2007) estimate the effect by converting snow cover to an equivalent thickness of rock and assuming that the snow has the same composition as the rock. The result of this assumption is that the dated surface occurs at a deeper effective depth closer to the peak in neutron flux, thereby driving increased production from capture on ^{6}Li. This simplification ignores the fact that snow is rich in nitrogen, giving it a much larger macroscopic absorption cross section than rock, potentially reducing the low-energy neutron flux at the surface of the rock.

Another reason the low-energy neutron flux estimated by Dunai et al. (2007) may be too high is the assumption of 3% water by mass (3300 ppm H) in the gneisses. This value is high compared with published values for Himalayan gneisses (400 to 1400 ppm), and increases the maximum low-energy neutron flux by 30–40% in a gneissic sample at an elevation of 4000 m (Brouand et al., 1990; Phillips et al., 2001). Thus, if the ^{3}He$_{cn}$ component is computed using the surface neutron flux and assuming a more appropriate ~650 ppm of H in the rock, the average corrected ^{3}He$_{c}$/^{10}Be ratio is ~31.3 giving a SLHL production rate of about 156 atoms g^{-1} yr^{-1} for garnet. This result agrees well with our estimate of 153 atoms g^{-1} yr^{-1} in garnet.

7. Conclusions

This study further demonstrates the feasibility of using apatite, zircon, and kyanite for cosmogenic ^{3}He dating. In particular, we have shown that small amounts of cosmogenic ^{3}He can be reliably measured in the presence of large amounts of radiogenic ^{4}He. Use of these mineral phases, as well as garnet (Gayer et al., 2004), and Fe–Ti oxides (Kober et al., 2005), can expand the variety of target lithologies suitable for cosmogenic ^{3}He dating.

Based on ^{3}He/^{10}Be systematics in Himalayan moraine boulders from 3–5 km elevation, we obtained apparent production rates of 226 atoms g^{-1} yr^{-1} in zircon, 254 atoms g^{-1} yr^{-1} in apatite, 177 atoms g^{-1} yr^{-1} in kyanite, and 153 atoms g^{-1} yr^{-1} in garnet. These results are surprising because they are significantly higher than production rates estimated by Farley et al. (2006) for apatite and zircon from comparable elevation in Bolivia. The unusually high production rate is also associated with increasing production rate with elevation. Both observations can be explained by an exponential increase in the ^{3}He/^{10}Be ratio with elevation, with a characteristic length scale of 4.2 km. If our result and that of Gayer et al. (2004) that different cosmogenic isotopes scale differently with altitude are general, then this may provide a new approach to paleoaltimetry.

At the present time, we do not favor a specific physical explanation for the observed trend. Further work is required to establish whether the same effect is seen outside the Himalayan region and over longer exposure intervals. For example, samples from a single ~100 kyr surface at 4 km in Bolivia (Farley et al., 2006) do not show the same effect, suggesting a geographically

or temporally complex behavior. It will also be important to compare ^{3}He production rates with those of cosmogenic isotopes other than ^{10}Be.

Acknowledgements

We thank Don Burnett for numerous helpful discussions. We also acknowledge funding from NSF award # 0511053.

Appendix A. Supplementary data

Supplementary data associated with this article can be found, in the online version, at doi:10.1016/j.epsl.2007.10.022.

References

Ackert, R.P., Singer, B.S., Guillou, H., Kaplan, M.R., Kurz, M.D., 2003. Long-term cosmogenic ^{3}He production rates from ^{40}Ar/^{39}Ar and K–Ar dated Patagonian lava flows at 47 degrees S. Earth Planet. Sci. Lett. 210, 119–136.

Andrews, J.N., Kay, R.L.F., 1982. Natural production of tritium in permeable rocks. Nature 298, 361–363.

Balco, G., Stone, J., in review. A simple, internally consistent, and easily accessible means of calculating surface exposure ages or erosion rates from ^{10}Be and ^{26}Al measurements. Quaternary Geochronology.

Barbey, P., Brouand, M., Le Fort, P., Pecher, A., 1996. Granite–migmatite genetic link: the example of the Manaslu granite and Tibetan Slab migmatites in central Nepal. Lithos 38, 63–79.

Bierman, P.R., 1994. Using in-situ produced cosmogenic isotopes to estimate rates of landscape evolution—a review from the geomorphic perspective. J. Geophys. Res.-Solid Earth 99, 13885–13896.

Blard, P.H., et al., 2006. Cosmogenic ^{3}He production rates revisited from evidence of grain size dependent release of matrix-sited helium. Earth Planet. Sci. Lett. 247, 222–234.

Bodemann, R., et al., 1993. Production of residual nuclei by proton-induced reactions on C, N, O, Mg, Al, and Si. Nucl. Instrum. Methods Phys. Res., B Beam Interact. Mater. Atoms 82, 9–31.

Brouand, M., Banzet, G., Barbey, P., 1990. Zircon behavior during crustal anatexis. Evidence from the Tibetan Slab migmatites (Nepal). J. Volcanol. Geotherm. Res. 44, 143–161.

Cerling, T., Craig, H., 1994. Cosmogenic ^{3}He production rates from 39N to 46N latitude, western USA and France. Geochim. Cosmochim. Acta 58, 249–255.

Chmiel, G., Fritz, S., Elmore, D., 2003. Control of ^{36}Cl production in carbonaceous shales by phosphate minerals. Geochim. Cosmochim. Acta 13, 2377–2395.

Colchen, M., Le Fort, P., Pecher, A., 1986. Geological research in the Nepal Himalaya, Annapurna–Manaslu–Ganesh Himal; notice of the geological map 1:200,000. Centre Nationale de la Recherche Scientifique, Paris.

Deniel, C., Vidal, P., Fernandez, A., Le Fort, P., Peucat, J., 1987. Isotopic study of the Manaslu granite (Himalaya, Nepal)––inferences on the age and source of Himalayan leucogranites. Contrib. Mineral. Petrol. 96, 78–92.

Dunai, T., Wijbrans, J., 2000. Long-term cosmogenic ^{3}He production rates (152 ka–1.35 Ma) from ^{40}Ar/^{39}Ar dated basalt flows at 29 degrees N latitude. Earth Planet. Sci. Lett. 176, 147–156.

Dunai, T., Stuart, F.M., Pik, R., Burnard, P.G., Gayer, E., 2007. Production of ^{3}He in crustal rocks by cosmogenic thermal neutrons. Earth Planet. Sci. Lett. 258, 228–236.

Farber, D.L., Hancock, G.S., Finkel, R.C., Rodbell, D.T., 2005. The age and extent of tropical alpine glaciation in the Cordillera Blanca, Peru. J. Quat. Sci. 20, 759–776.

Farley, K.A., Liabarkin, J., Mukhopadhyay, S., Amidon, W., 2006. Cosmogenic and nucleogenic ^{3}He in apatite, titanite, and zircon. Earth Planet. Sci. Lett. 248, 436–446.

Friedlander, G., Kennedy, J.W., Macias, E.S., Miller, J.M., 1981. Nuclear and Radiochemistry. John Wiley & Sons, New York.

Garzanti, E., Gorza, M., Martenelli, L., Nicora, A., 1994. Transition from diagenesis to metamorphism in the Paleozoic to Mesozoic succession of the Dolpo-Manang synclinorium and Thakkhola Graben (Nepal Tethys Himalaya). Eclogae geol. Helv. 87, 613–632.

Gayer, E., et al., 2004. Cosmogenic ^{3}He in Himalayan garnets indicating an altitude dependence of the ^{3}He/^{10}Be production ratio. Earth Planet. Sci. Lett. 229, 91–101.

Gayer, E., Lavé, J., Pik, R., France-Lanord, C., 2006. Monsoonal forcing of Holocene glacier fluctuations in Ganesh Himal (Central Nepal) constrained by cosmogenic ^{3}He exposure ages of garnets. Earth Planet. Sci. Lett. 252, 275–288.

Gehrels, G.E., et al., 2003. Initiation of the Himalayan Orogen as an early Paleozoic thin-skinned thrust belt. GSA Today 13, 4–9.

Goldhagen, P., et al., 2002. Measurement of the energy spectrum of cosmic-ray induced neutrons aboard an ER-2 high-altitude airplane. Nucl. Instrum. Methods Phys. Res., Sect. A, Accel. Spectrom. Detect. Assoc. Equip. 476, 42–51.

Gosse, J., Phillips, F., 2001. Terrestrial in situ cosmogenic nuclides: theory and application. Quat. Sci. Rev. 20, 1475–1560.

Guillot, S., Le Fort, P., 1995. Geochemical constraints on the bimodal origin of High Himalayan leucogranites. Lithos 35, 221–234.

Heisinger, B., Lal, D., Jull, A.J.T., Kubik, P.W., Ivy-Ochs, S., Neumaier, S., Knie, K., Lazarev, V., Nolte, E., 2002. Production of selected cosmogenic radionuclides by muons: 1. fast muons. Earth Planet. Sci. Lett. 200, 345–355.

House, M.A., Farley, K.A., Stockli, D., 2000. Helium chronometry of apatite and titanite using Nd-YAG laser heating. Earth Planet. Sci. Lett. 183, 365–368.

Kober, F., et al., 2005. In situ cosmogenic ^{10}Be and ^{21}Ne in sanidine and in situ cosmogenic ^{3}He in Fe–Ti-oxide minerals. Earth Planet. Sci. Lett. 236, 404–418.

Kurz, M.D., Colodner, D., Trull, T.W., Moore, R.B., Obrien, K., 1990. Cosmic-ray exposure dating with in-situ produced cosmogenic He-3-results from young Hawaiian lava flows. Earth Planet. Sci. Lett. 97, 177–189.

Lal, D., 1987. Production of ^{3}He in terrestrial rocks. Chem. Geol. 66, 89–98.

Lal, D., 1991. Cosmic ray labeling of erosion surfaces: in situ production rates and erosion models. Earth Planet. Sci. Lett. 104, 424–439.

Lal, D., Peters, B., 1967. Cosmic ray produced radioactivity in the earth. Handbuch der Physik. Springer-Verlag, pp. 551–612.

Le Fort, P., 1981. Manaslu leucogranite: a collision signature of the Himalaya a model for its genesis and emplacement. J. Geohpys. Res. 86, 10545–10568.

Leya, I., et al., 1998. Measurement of cross sections for the proton-induced production of helium and neon isotopes from magnesium, aluminum, and silicon. Meteorit. Planet. Sci. 33, A94–A94.

Leya, I., et al., 2000a. Simulation of the interaction of galactic cosmic-ray protons with meteoroids: On the production of radionuclides in thick gabbro and iron targets irradiated isotropically with 1.6 GeV protons. Meteorit. Planet. Sci. 35, 287–318.

Leya, I., Lange, H.J., Neumann, S., Wieler, R., Michel, R., 2000b. The production of cosmogenic nuclides in stony meteoroids by galactic cosmic-ray particles. Meteorit. Planet. Sci. 35, 259–286.

Licciardi, J., Kurz, M.D., Clark, P., Brook, E., 1999. Calibration of cosmogenic ^{3}He production rates from Holocene lava flows in Oregon, USA, and effects of the Earth's magnetic field. Earth Planet. Sci. Lett. 172, 261–271.

Licciardi, J.M., Kurz, M.D., Curtice, J.M., 2006. Cosmogenic ^{3}He production rates from Holocene lava flows in Iceland. Earth Planet. Sci. Lett. 246, 251–264.

Mamyrin, B.A., Tolstikhin, I.N., 1984. Helium Isotopes in Nature. Elsevier, Amsterdam.

Masarik, J., 2002. Numerical simulation of in-situ production of cosmogenic nuclides. Geochim. Cosmochim. Acta 66, 491.

Michel, R., et al., 1997. Cross sections for the production of residual nuclides by low-and medium-energy protons from the target elements C, N, O, Mg, Al, Si, Ca, Ti, V, Mn, Fe, Co, Ni, Cu, Sr, Y, Zr, Nb, Ba and Au. Nucl. Instrum. Methods Phys. Res., B Beam Interact. Mater. Atoms 129, 153–193.

Michel, R., et al., 1995. Nuclide production by proton-induced reactions on elements ($6<Z<29$) in the energy-range from 800 to 2600 MeV. Nucl. Instrum. Methods Phys. Res., B Beam Interact. Mater. Atoms 103, 183–222.

Owen, L.A., et al., 2005. Climatic and topographic controls on the style and timing of late Quaternary glaciation throughout Tibet and the Himalaya defined by ^{10}Be cosmogenic radionuclide surface exposure dating. Quat. Sci. Rev. 24, 1391–1411.

Phillips, F., Plummer, M.A., 1996. A program for reinterpreting in-situ cosmogenic nuclide data for surface exposure dating and erosion studies. Radiocarbon 38, 98–99.

Phillips, F., Stone, W.D., Fabryka-Martin, J.T., 2001. An improved approach to calculating low-energy cosmic ray neutron fluxes near the land/atmosphere interface. Chem. Geol. 175, 689–701.

Pigati, J.S., Lifton, N.A., 2004. Geomagnetic effects on time-integrated cosmogenic nuclide production with emphasis on in situ ^{14}C and ^{10}Be. Earth Planet. Sci. Lett. 226, 193–205.

Potts, P.J., Tindle, A.G., Webb, P.C., 1992. Geochemical Reference Material Compositions. CRC Press, Ann Arbor.

Pratt-Sitaula, B., 2004. Glaciers, Climate, and Topography in the Nepalese Himalaya, UC Santa Barbara, Santa Barbara. 152 pp.

Sato, T., Niita, K., 2006. Analytical functions to predict cosmic-ray neutron spectra in the atmosphere. Radiat. Res. 166, 544–555.

Schiekel, T., et al., 1996. Nuclide production by proton-induced reactions on elements ($6<Z<29$) in the energy range from 200 MeV to 400 MeV. Nucl. Instrum. Methods Phys. Res., B Beam Interact. Mater. Atoms 114, 91–119.

Schneider, C., Masch, L., 1993. The metamorphism of the Tibetan Series from the Manang area, Marsyandi Valley, Central Nepal. In: Treloar, P.J., Searle, M.P. (Eds.), Himalayan Tectonics. Geological Society of London, London, pp. 357–374.

Searle, M.P., Godin, L., 2003. The South Tibetan Detachment and the Manaslu Leucogranite: a structural reinterpretation and restoration of the Annapurna-Manaslu Himalaya, Nepal. J. Geol. 111, 505–523.

Young, E., Myers, A., Munson, E., Conklin, N., 1969. Mineralogy and geochemistry of fluorapatite from Cerro de Mercado, Durango, Mexico. U. S. Geol. Surv. Prof. Pap. 650-D, 84–93.